IEEE Access
Multidisciplinary ⋮ Rapid Review ⋮ Open Access Journal

Received February 8, 2022, accepted March 22, 2022, date of publication March 25, 2022, date of current version April 1, 2022.

Digital Object Identifier 10.1109/ACCESS.2022.3162272

Universal Convolutional Neural Network for Histology-Independent Analysis of Collagen Fiber Organization in Scar Tissue

THI TRAM ANH PHAM[1], HYEONSOO KIM[2], YEACHAN LEE[2], HYUN WOOK KANG[2,3], AND SUHYUN PARK[1], (Member, IEEE)

[1]Department of Electronic and Electrical Engineering, Ewha Womans University, Seoul 03760, South Korea
[2]Department of Industry 4.0 Convergence Bionics Engineering, Pukyong National University, Busan 48513, South Korea
[3]Marine-Integrated Biomedical Technology Center, Department of Biomedical Engineering, Pukyong National University, Busan 48513, South Korea

Corresponding authors: Hyun Wook Kang (wkang@pukyong.ac.kr) and Suhyun Park (suhyun.park@ewha.ac.kr)

This work was supported in part by the Korea Medical Device Development Fund Grant funded by the Korea Government (the Ministry of Science and ICT, the Ministry of Trade, Industry and Energy, the Ministry of Health & Welfare, and the Ministry of Food and Drug Safety) under Project 202016B01; and in part by the Basic Science Research Program through the National Research Foundation of Korea (NRF) funded by the Ministry of Science and ICT under Grant NRF-2020R1A2C1011889.

This work involved animals in its research. Approval of all ethical and experimental procedures and protocols was granted by the Institutional Animal Care and Use Committee at Pukyong National University under Application No. PKNUIACUC-2019-31.

ABSTRACT Histological examination of collagen fiber organization is essential for pathologists to observe the wound healing process. A convolutional neural network (CNN) can be utilized to visually analyze collagen fibers during tissue remodeling in histology images. In this study, a universal CNN (UCNN) independent of the histological staining process is proposed to classify the histology images of burn-induced scar tissues and characterize collagen fiber organization. Normal and scar tissues obtained from an in vivo rodent model are stained using Masson's Trichrome (MT) and Hematoxylin & Eosin (H&E). The proposed universal model is trained using both MT- and H&E-stained histological image datasets over multiple scales with color augmentation, and classification accuracies of up to 98% and 97% are achieved for the MT- and H&E-stained image datasets, respectively. Regardless of the histological staining process used, the collagen characteristics are visualized by determining the density and directional variance of the normal and scar tissues by using the features extracted with the proposed universal model. Statistical analysis results demonstrated clear differences between scar and normal tissues in terms of collagen fiber organization. The proposed UCNN model can contribute to the development of an intelligent and efficient method that pathologists can use to rapidly evaluate wound healing and tissue remodeling.

INDEX TERMS Histology image, collagen fiber characterization, scar tissue classification, convolutional neural network, hue-saturation specificity analysis.

I. INTRODUCTION

Dermal wound healing is a dynamic process that can be triggered by thermal tissue injury. It involves complex interactions between dermal cells and the extracellular matrix (ECM) [1]–[3]. The wound healing process essentially comprises three overlapping phases: inflammatory, proliferative, and remodeling [3], [4]. The characteristics of collagen constitute an index that can be used to quantify the wound healing process. Collagen is initially synthesized in the proliferation phase by fibroblasts and myofibroblasts. Collagen accumulation provides strength to healing tissues, and the shape, quantity, and organization of collagen fibers change gradually during tissue remodeling. Scar tissue is the connective tissue that forms over a wound during the wound healing process. The most prominent differences between scar tissue and normal tissue are the appearance of covalent cross-linking and the amount of collagen fiber in the tissue. Dense distribution and aligned orientation of collagen fibers are considered as the main characteristics of scar tissue [5]. It is critical to

The associate editor coordinating the review of this manuscript and approving it for publication was Tao Zhou.

evaluate the changes in the morphology and organization of collagen fibers to assess the wound healing process and establish methodologies for various medical approaches and therapeutic interventions.

Histology is the study of tissues through staining and microscopic examination [6], [7]. The method can reveal remarkable bioinformatics, such as microstructural features. For this reason, several histological studies have been conducted to derive biomarkers for prognosis and diagnosis [8], [9]. Histological staining methods enhance the hue contrast of various tissue constituents under a microscope without distorting the structure of a tissue specimen. Histological images have been utilized to semantically segment biological components (e.g., stroma, nuclei, and cytoplasm) that are the most relevant for cancer diagnosis [10], [11]. Several histological stains are available, for instance, Hematoxylin & Eosin (H&E) and Masson's Trichrome (MT) [12]–[14]. The H&E staining method is the most widely used tissue staining method owing to its simplicity and low cost. In H&E-stained histological images, nuclei are stained dark blue owing to their hematoxyphilia, and the cytoplasm and ECM are stained varying shades of pink owing to their eosinophilia [6], [15]. Because collagen is one of the substances deposited in the extracellular compartment, collagen fibers and matrices can be stained different shades of pink [15] in H&E-stained histology images. In MT-stained histology images, collagen is stained blue or green, and other skin appendages including hair follicles, sebaceous glands, and granules are stained shades of red and purple [7]. In histology images, color is an important discriminator of specific stained structures in tissues. Although the color of collagen fibers is not clearly differentiated with H&E staining, it is easily discriminated from other tissue structures with MT staining. Quinn *et al.* (2014) introduced an image processing method to quantify the density and directional variance of collagen fibers during the wound healing process of cutaneous burns by using MT-stained histology images [14]. To quantify and characterize the organization of collagen in tissue, various microscopy techniques, such as conventional light microscopy, confocal microscopy, second harmonic generation microscopy, and multiphoton fluorescence microscopy, have been used [16]–[23]. Macros-Garces *et al.* (2017) measured collagen bundle orientations in samples processed using different staining and microscopy techniques, including H&E staining with confocal microscopy [23]. Fereidouni *et al.* (2019) investigated brightfield (BF) and fluorescence images of H&E-stained tissue samples to highlight the collagen distribution in them by conducting spectral phasor analysis [24].

Deep learning (DL) techniques have contributed greatly to the current biomedicine revolution [25]–[30]. DL can be used to extract complex patterns from annotated clinical datasets for solving numerous diagnostic tasks, such as disease diagnosis, treatment selection, and patient monitoring [8], [31]. In medical image analysis, convolutional neural networks (CNNs) have been widely used and have yielded promising results in terms of computer-aided diagnostics, segmentation, and object detection [31], [32]. Computational pathology has been utilized to analyze tissues corresponding to distinct biological features such as tumors or stroma [15], [33]. Keikhosravi *et al.* (2020) utilized an autoencoder to synthesize collagen-specific images from BF images of H&E-stained tissue samples [11]. To avoid variations in the process of histology imaging, such as the imaging system and staining manipulation, color augmentation and normalization were introduced [33]–[37]. Tellez *et al.* (2019) developed a CNN model based on color augmentation by varying the brightness, contrast, and hue-saturation-value (HSV) transformation to classify H&E-stained slides acquired from multiple sites [34].

In a previous study, we proposed a CNN model trained using MT-stained histology images to classify normal tissue and scar tissue and to characterize collagen fiber organization (i.e., density and directional variance) [13]. Although various staining methods can be used for histology imaging, the biological structures in tissue are consistent. Thus, it is expected that the corresponding histology images can be differentiated, regardless of the colors of the structures in a tissue sample. In this study, we propose a universal CNN (UCNN) model that can be applied to both MT-stained and H&E-stained histology images. This model can distinguish between normal tissue and scar tissue, and it can visually characterize the microstructure of collagen fibers (density and directional variance). Because the main difference between the two staining methods is the color feature, we perform color augmentation and hue saturation specificity analysis. A burn injury is initially induced by applying laser irradiation to in vivo rodent models. Both MT- and H&E-stained histology images of the resulting scar tissue on the skin are captured after four weeks of wound healing. The classification and characterization performances of the proposed UCNN model are evaluated using the MT- and H&E-stained histology images, including individual normal and scar tissue images and the whole histology images.

II. MATERIALS AND METHODS

A. ANIMAL SCAR MODEL AND STAINED HISTOLOGY IMAGES

In the experiments, we used eight male Sprague Dawley rats (age = 7 weeks, weight = 200–250 g) to generate an in vivo scar model. The Institutional Animal Care and Use Committee at Pukyong National University approved all the animal tests conducted in this study (Number PKNUIACUC-2019-31). Each animal was anesthetized with 3% isoflurane (Terrell isoflurane, Piramal Critical Care, Bethlehem, PA, USA) by using a respiratory anesthesia system (Classic T3, SurgiVet, USA) in a chamber. The scar model was created by irradiating the back of each rat with a high-power laser light to induce a thermal burn on the skin through photothermal interactions. Before laser irradiation, the hair on the back of each rat was removed using an electric hair clipper and

waxing cream (Nair Sensitive Hair Removal Cream, Nair, Australia) to maximize light absorption by the skin tissue. As a light source, a 1470-nm laser system (FC-W-1470, CNI Optoelectronics Tech. Co., China) was used to generate burn-induced scars in the in vivo models. Because of strong light absorption by water (absorption coefficient = 28.4 cm^{-1}), the selected wavelength led to a short optical penetration depth in the skin, which limited the thermal burn to within the dermal layer. A 600-μm end-firing optical fiber was placed 25 mm vertically above the skin surface (beam size = 0.3 cm^2) to deliver the laser light. Perpendicular irradiation created a circular-shaped thermal burn on the skin with a diameter of 10 mm. To reliably establish the burn wound without carbonization, we applied a laser power of 5 W for 30 s on the skin surface (i.e., corresponding irradiance = 16.7 W/cm^2). Four weeks after irradiation, because the wound healing process was complete, a mature hypertrophic scar was fully developed in each animal.

Burn-induced scar tissue samples were harvested from all of the animals after complete tissue re-epithelialization by the ECM. Initially, all samples were fixed in 10% formalin for 48 hours. Then, paraffin blocks were prepared and sliced to a thickness of 5 μm to prepare histology slides (N = 10 slides per block). All histology slides were stained with two different histochemical dyes: MT and H&E (American MasterTech, California, USA). A Motic Digital Slide Assistant System was used to acquire high-resolution microscopy images of the histology slides (MoDSA, Richmond, British Columbia, Canada; 40X and 0.26 μm/pixel resolution). The acquired MT- and H&E-stained histology images (14269 × 6637 and 15059 × 4735 pixels, respectively) of the wounded skin are shown in Figs. 1(a) and (b), respectively. The histology images display the regions of interest (ROIs), namely the normal region (ROI; orange dashed box on the left and right sides) and the scar region (ROI; orange dashed box in the middle of the image). The normal region consists of coarse collagen fibers, whereas the scar region consists of fine collagen fibers. In the MT-stained histology image (Fig. 1(a)), the collagen fibers are stained blue, which distinguishes them from the other structures (e.g., sweat glands, sebaceous glands, and hair follicles) stained red or purple. Meanwhile, in Fig. 1(b), the collagen fibers are mostly stained pink or purple, which makes it challenging to differentiate them from appendages owing to their similarity on the color spectrum.

B. DEEP LEARNING APPROACH

1) PROPOSED UCNN MODEL

Fig. 2 presents a block diagram of the proposed UCNN model for classifying normal and scar tissues and characterizing collagen fibers. The architecture of the proposed UCNN model is identical to that of the model proposed in our previous study [13]. In this study, we trained the model by using MT- and H&E-stained histology images. Because the proposed model is effective when applied to histology images acquired using both staining methods, we call it the universal CNN (UCNN) model. The histology images (Fig. 2(a)) were resized to the input size of the model (224 × 224 pixels) by means of bilinear interpolation and normalized to [0, 1] with respect to each channel for preprocessing (Fig. 2(b)). The model comprises three blocks of stacked convolution layers. The first two blocks consist of two convolution layers and a max-pooling layer each. The last block consists of a convolution layer, global average pooling (GAP) layer, dropout layer, and sigmoid classifier. The GAP layer acts as a structural regularizer, and the dropout layer is used to prevent overfitting. The architecture of the proposed model is illustrated in Fig. 2(c). A sigmoid classifier is employed in the last layer to classify normal tissue and scar tissue by ensuring that the output score lies in the interval [0, 1] (Fig. 2 (d)).

2) DATA GENERATION

As summarized in Table 1, the MT- and H&E-stained histology image datasets of the two labeled groups (normal and scar) with image sizes of 250 × 250 pixels (560 images in each group) and 500 × 500 pixels (120 images in each group) were prepared to train the proposed model. For augmentation, the images were rotated to 18 different angles (from 5° to 180° in increments of 10°) to change the angle of the collagen bundles. Moreover, they were flipped along the horizontal and/or vertical directions. The basic augmented data of 10,400 images (5,200 images each of normal and scar tissues) were generated. Then, to mimic the color and illumination variations due to the staining process and image acquisition, random color variation, including changes to brightness and contrast in the ranges of [0.8–1.2] and [0.9–1.1], were applied to the MT- and H&E-stained images, respectively. Then, the images were further augmented in the HSV color space by shifting hue and value in the range of [0.95–1.05] and saturation in the range of [0.5–1.5] for MT images and by shifting the value channel in the range of [0.8–1.8] for H&E images. Then, the augmented images were reconverted to the RGB color space for training and validation purposes. Fig. 3 shows the augmentation process used to generate the training data for the proposed UCNN model. The training and validation data were utilized in the ratio of 7:3. To avoid overfitting and optimize the training hyperparameters (e.g., learning rate and number of epochs), loss of validation data during the training process was monitored.

TABLE 1. Training and test data.

Purpose	Size (pixel × pixel)	Each staining dataset		
		Normal	Scar	Whole
Training	250 × 250	280	280	
	500 × 500	60	60	
Test	500 × 500	690	690	
	1000 × 500	345	345	
	1017 × 1920	115	115	
	Not specified			21
Total test		1150	1150	21

To test the proposed model, three sets of images of different sizes (500 × 500, 1000 × 500, and 1017 × 1920 pixels) were

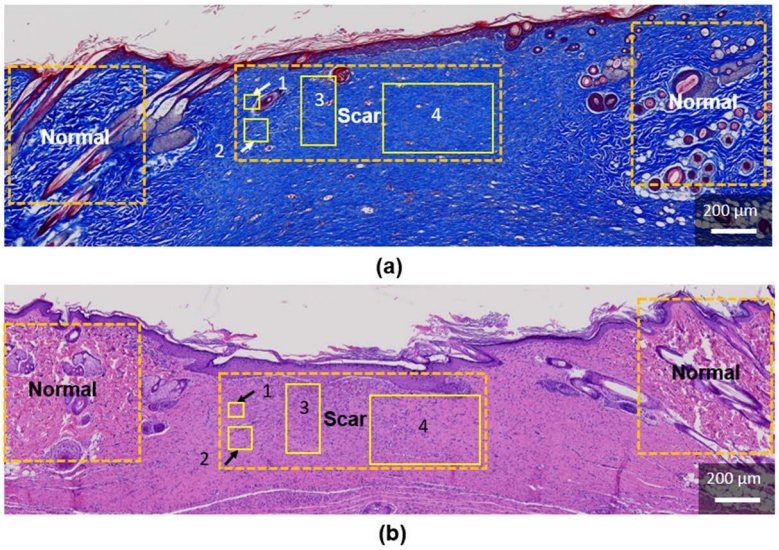

FIGURE 1. Photomicrograph of wounded skin tissue stained with (a) MT, (b) H&E. The orange-dashed boxes on the left and right sides show the normal tissue regions (as the control) that consist of coarse collagen fibers with skin appendages. The orange dashed box in the middle of the image represents the burn-induced scar tissue region with fine collagen fibers. The three solid yellow boxes inside the scar region are examples of ROIs of various sizes (1: 250 × 250 pixels, 2: 500 × 500 pixels, 3: 1000 × 1000, and 4: 1017 × 1920 pixels; bar = 200 μm; 40X).

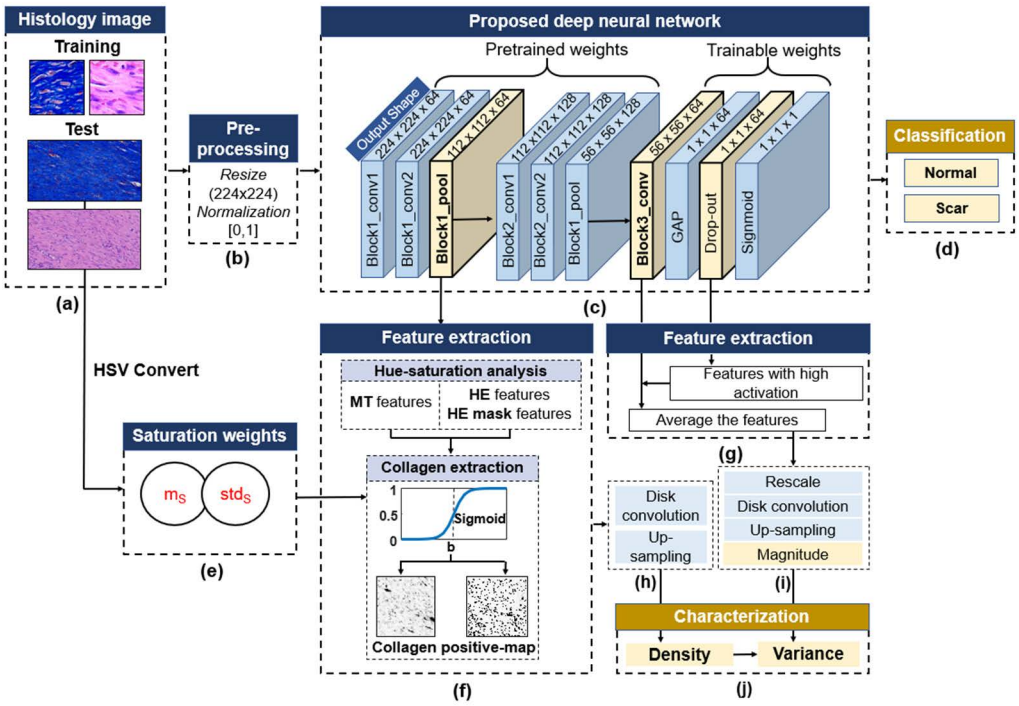

FIGURE 2. Block diagram of proposed UCNN model, and processes for classification and characterization: (a) Training and test images used for the proposed model, (b) pre-processing, (c) proposed UCNN model, (d) classification, and (e–j) feature extraction and characterization.

prepared, and these sets contained 1380, 690, and 230 images, respectively. In addition to the individual normal and scar histology images, 42 whole histology images containing both normal and scar regions were utilized (21 for each staining method).

3) MODEL TRAINING AND TEST

The parameters of first two blocks of the proposed UCNN model were initialized using the pre-trained weights of VGG-16 (VGG: Visual Geometry Group, 16: number of learnable parameter layers) by using the ImageNET

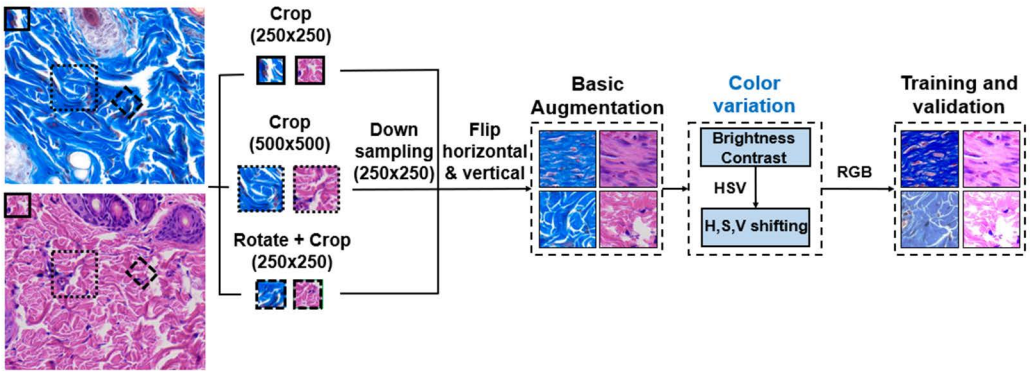

FIGURE 3. Augmentation process to generate the training dataset.

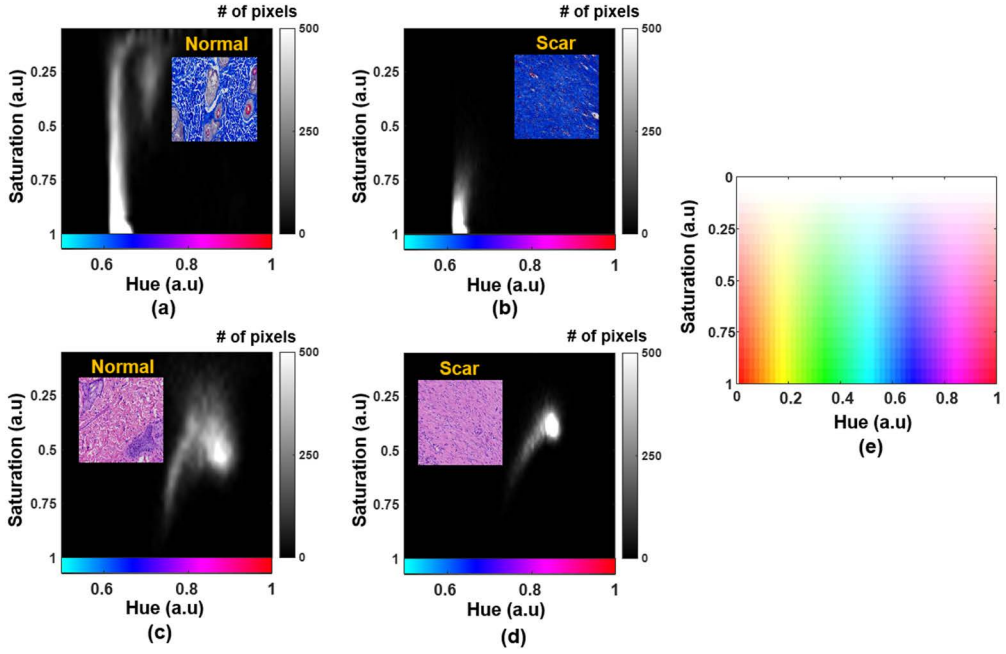

FIGURE 4. Two-dimensional histogram of hue and saturation channels corresponding to MT-stained histology images of (a) normal and (b) scar tissues, and H&E-stained histology images of (c) normal and (d) scar tissues. (e) Monochrome representation with varying hue and saturation (#: number).

dataset [38]. The parameters of the last convolution layers and the sigmoid layer of the model were initialized by means of Xavier random initialization. The parameters of the proposed UCNN model were trained using both MT- and H&E-stained histology images (Table 1).

Table 2 lists the hyperparameters used to train the UCNN model. An Adam optimizer with a learning rate of 0.0001 was used. A binary cross-entropy loss function was applied for classification. The regularizer L2 imposed penalties on the last convolution layer and the sigmoid layer during optimization. The number of epochs was 75, and the process was stopped early when no improvement in validation loss was observed over the last 10 epochs. The batch size of the model was 10. The model was trained and tested on a computer equipped with an Intel®Core™i7-8700 CPU @ 3.2 GHz, NVIDIA GeForce GTX 1050 Ti graphical processing unit (GPU), Python 3.7.9, and the Keras module within TensorFlow 1.14.0.

4) PERFORMANCE EVALUATION

The proposed UCNN model was compared to EfficientNetB0, EfficientNetB2 [39], and support vector machine (SVM) [40]. EfficientNetB0 and EfficientNetB2 were initialized with the weights pre-trained using the ImageNET dataset, and the last sigmoid layer was trained using both MT- and H&E-stained histology images (Table 1). In the case of SVM, features were extracted and quantized using the scale-invariant feature transform (SIFT) algorithm [41]

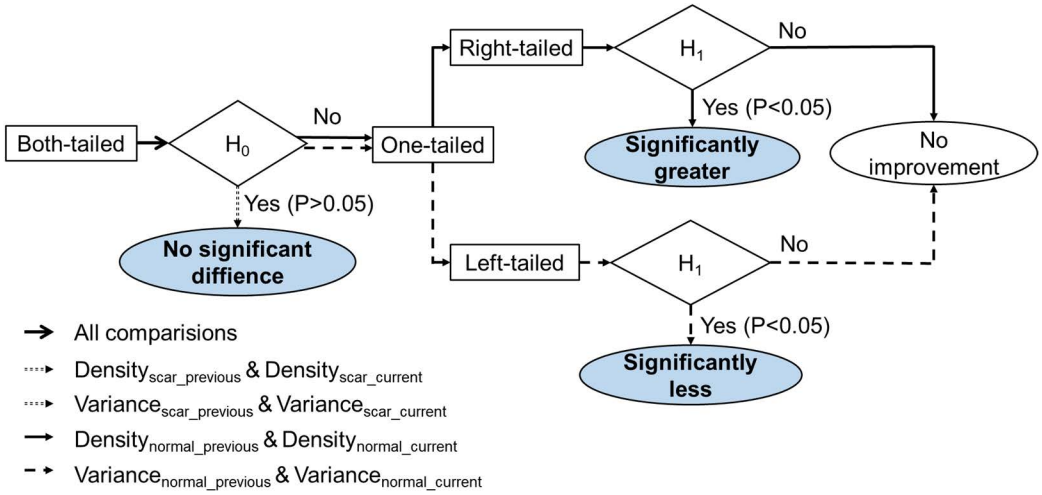

FIGURE 5. Flowchart of statistical analysis for characterization of density and variance of scar and normal tissues (All comparisons: density and variance of normal and scar tissues obtained in our previous and current studies. _previous: values obtained in our previous study and _current: values obtained in the present study).

TABLE 2. Configuration of training process.

Hyperparameters	UCNN
Loss function	Binary cross-entropy
Optimizer	Adam
Regularizer	L2
Learning rate	0.0001
Number of epochs	75
Batch size	10
Drop-out probability	0.5

and K-means clustering algorithm, respectively [42]. Then, a bag of features was used to reconstruct the main features for SVM to distinguish between normal tissue and burn tissue in histology images [43]. The SVM was configured as follows: regularization parameter 40 and Gaussian kernel with scale gamma 0.002.

To evaluate the classification performance of the proposed model, its accuracy, precision, recall, receiver operating characteristics (ROC), area under the curve (AUC), and confusion matrix were obtained using the test data presented in Table 1 [44]. For EfficientNetB0 and SVM, accuracy, precision, and recall were measured to compare their classification performances with that of the proposed method.

5) HUE-SATURATION SPECIFICITY ANALYSIS

Fig. 4 shows the hue and saturation spectra of the MT- (Figs. 4(a) and (b)) and H&E-stained (Figs. 4(c) and (d)) histology images of normal and scar tissues. The collagen part occupies a vast area in the histology images of the scar tissue. Histograms of the hue spectra indicate that the majority of the color spectrum of the MT-stained histology image is in the blue range (i.e., corresponding color hue: 0.55–0.65) while that of the H&E-stained histology images is in the pink range (i.e., corresponding color hue: 0.75–0.95). The saturations of the MT- and H&E-stained histology images lie in the range of [0.75–1] and [0.25–0.6], respectively. A hue-saturation specificity analysis was performed to analyze the color sensitivity of each neuron in the trained UCNN model to select filters for collagen extraction [45]. One thousand monochrome images were generated by varying the hue between 0 and 1 in increments of 0.02 [45] and the saturation between 0 and 1 in increments of 0.05, as well as fixing the value to 1 by following the monochrome representation in Fig. 4(e). Then, the generated monochrome images were used as input images for the trained UCNN model to realize monochrome activation in the hue-saturation specific feature extraction process.

6) CHARACTERIZATION OF COLLAGEN FIBERS

a: COLLAGEN DENSITY

Figs. 2 (e), (f), (h), and (j) illustrate the process of extracting collagen characteristics by using the features obtained from the pooling layer in block 1 (first yellow box in Fig. 2(c)) in the proposed model. Feature numbers were assigned according to the filter training order, which represents the order in the third dimension of the output of each layer (Fig. 2 (c)). For the MT- and H&E-stained images, features 8, 28, and 53 and features 19, 46, and 53, respectively, were utilized to extract collagen-dense regions in the images based on the results of hue-saturation specific analysis. Because appendage structures exhibited higher levels of activation in the H&E-stained histology images, an additional mask was generated following Otsu's method [46] by using features 3 and 52 for appendage removal. After averaging the features, the collagen-positive map (CP) was generated as follows:

$$CP\,(m_a) = 1/(1 + e^{-20*(m_a - b)}) \quad (1)$$

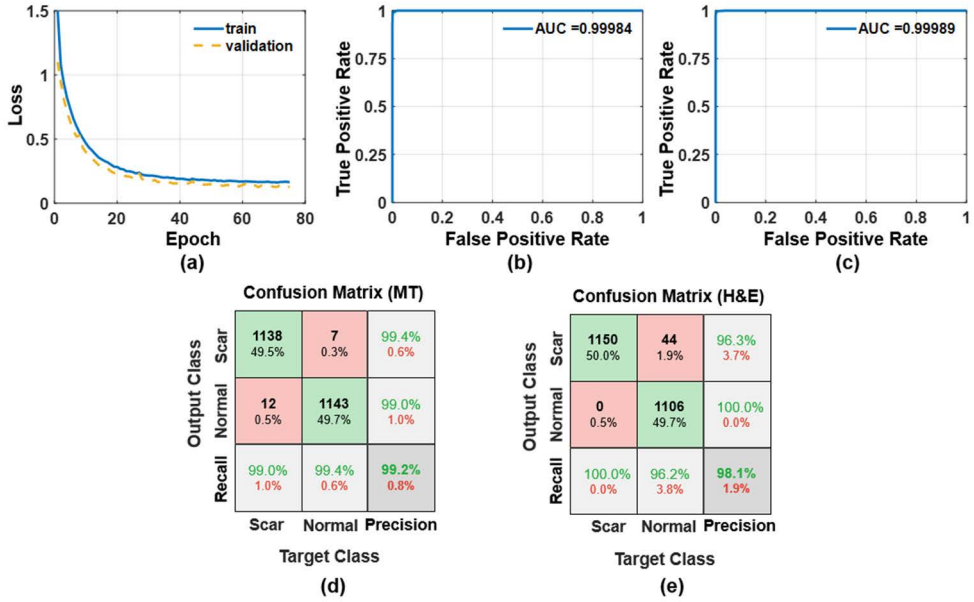

FIGURE 6. (a) Learning curve of proposed UCNN, ROC curves of (b) MT- and (c) H&E-stained histology images, and confusion matrix of (d) MT- and (e) H&E-stained histology images.

where m_a is the average activation of the selected feature maps, and b is calculated by means of multiple linear regression between the saturation of the original image and the averaged feature map, as follows:

$$b = k_1 * (m_s + 0.5 * std_s) + k_2 * std_f + k_3 \tag{2}$$

where m_s and std_s denote the mean and standard deviation extracted from the saturation (Fig. 2(e)), respectively; std_f is the standard deviation of the averaged feature map; k_1 and k_2 are slope coefficients, and k_3 is a bias, which are calculated by fitting a plane to the means of average activation (m_f), statistical representations of saturation (m_s and std_s), and standard deviations of the average activation (std_f). The values of (k_1, k_2, k_3) are (0.15, 0.95, 0.29) and (0.59, 0.95, 0.17) for the MT- and H&E-stained images, respectively. To calculate the local collagen density, the collagen-positive map was convolved with the disk kernel [14]. The disk kernel size was adjusted according to the size of the input image. Finally, the density map $D(x, y)$ was obtained by up-sampling to the original image size by means of bicubic interpolation.

b: DIRECTIONAL VARIANCE

Six of the most strongly activated features of the last convolution layer in the proposed UCNN model (block3_conv in Fig. 2(g)) were utilized owing to their directional filter patterns and high levels of contribution to the classification decision [13]. Figs. 2(g), (i), and (j) represent the process of calculating the directional variance. The magnitude map $M(x, y)$ was calculated as follows:

$$M(x, y) = (1/N) * \sum f_i(x, y) \tag{3}$$

where $f_i(x, y)$ is the ith normalized feature map of the convolution layer of block 3, where $i \in \{4,14,41,45,46,53\}$, and N is the number of selected features. The resultant map was convolved with the disk kernel and resized to the original image size by means of bicubic interpolation. Then, the directional variance map $V(x, y)$ was generated by normalizing the magnitude of collagen pixel density, as follows (Fig. 2(j)):

$$V(x, y) = 1 - M(x, y)/D(x, y) \tag{4}$$

c: STATISTICAL ANALYSIS

The differences in density and directional variance between normal tissue and scar tissue were examined using Wilcoxon signed rank statistics, where $p < 0.05$ was considered statistically significant [47], [48]. The results of our previous work involving MT-stained histology images and those of the present work involving MT- and H&E-stained histology images were compared. To evaluate the differences in density and directional variance between the previous and current studies, we conducted a two-tailed hypothesis test. The null hypothesis (H0) was that there is no significant difference between the mean values of density and directional variance extracted in the previous study and those extracted using the approach proposed in the present study. To investigate whether there was an improvement in the characterization performance of the approach proposed in the current study, a one-tailed hypothesis test was conducted to compare the mean values of normal and scar tissues in terms of density and directional variance. In the one-tailed test, an alternative hypothesis (H1) was employed to demonstrate that density or directional variation in the normal tissue extracted using the previous approach was significantly greater than or less than

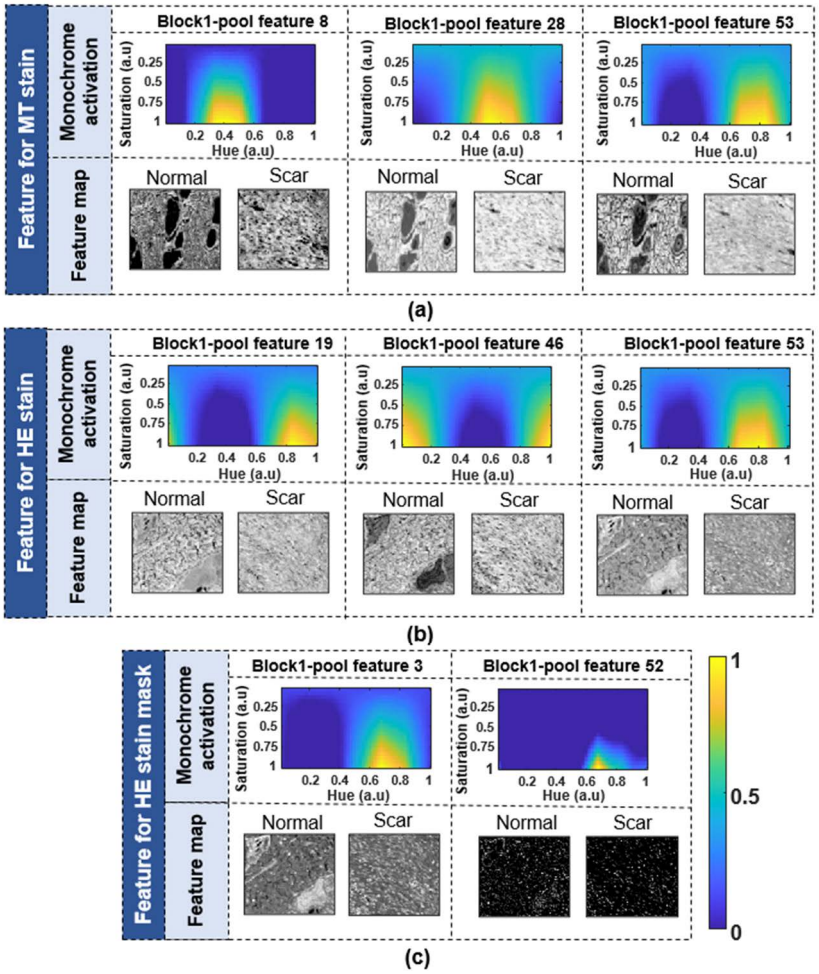

FIGURE 7. Monochrome activations obtained using the proposed UCNN model and the corresponding feature maps of the selected filters for (a) MT- (b) H&E-stained histology images, and (c) additional mask for H&E-stained image.

that extracted using the proposed approach. Moreover, a one-tailed test was conducted to indicate any significant decrease or increase in density and directional variance between normal and scar tissues when applying the proposed approach to MT- and H&E-stained histology images. Fig. 5 shows the flowchart of the statistical analysis performed herein to evaluate the performance of the proposed approach in characterizing the density and variance of normal and scar tissues.

III. RESULTS

A. CLASSIFICATION OF NORMAL AND SCAR IMAGES

Fig. 6 shows the learning curves obtained during training (Fig. 6(a)), ROC curves of MT- and H&E-stained histology images (Figs. 6(b) and (c)), and confusion matrices of the proposed model for each staining method (Figs. 6(d) and (e)).

Table 3 summarizes the classification performance of SVM, EfficientNetB0, EfficientNetB2, and the proposed UCNN model for MT- and H&E-stained histological datasets. The proposed UCNN model achieved accuracies of 98.7% and 97.9% in the classification of MT- and H&E-stained image, respectively. Both EfficientNetB0 and EfficientNetB2 performed good quantitative results for H&E-stained images (accuracies 97.8% and 99.5%, respectively), but not for MT-stained images (accuracies 94.1% and 92.8%, respectively). The proposed UCNN model outperformed SVM by 9.9% and 11.3% in terms of classification accuracy when applied to MT- and H&E-stained images, respectively. Overall, the proposed model achieved superior precision and recall for both MT- and H&E-stained images. Thus, the features extracted using the proposed model with strong classification performance can expectedly be used to characterize the collagen properties of both MT- and H&E-stained histology images.

TABLE 3. Comparison of classification performance of models.

Staining method	Metric	SVM	EfficientNet B0	EfficientNet B2	UCNN
MT	Accuracy (%)	88.8	94.1	92.8	**98.7**
	Precision	0.893	0.950	0.941	**0.987**
	Recall	0.888	0.941	0.928	**0.987**
H&E	Accuracy (%)	86.6	97.8	**99.5**	97.9
	Precision	0.876	0.98	**0.995**	0.981
	Recall	0.869	0.978	**0.995**	0.979

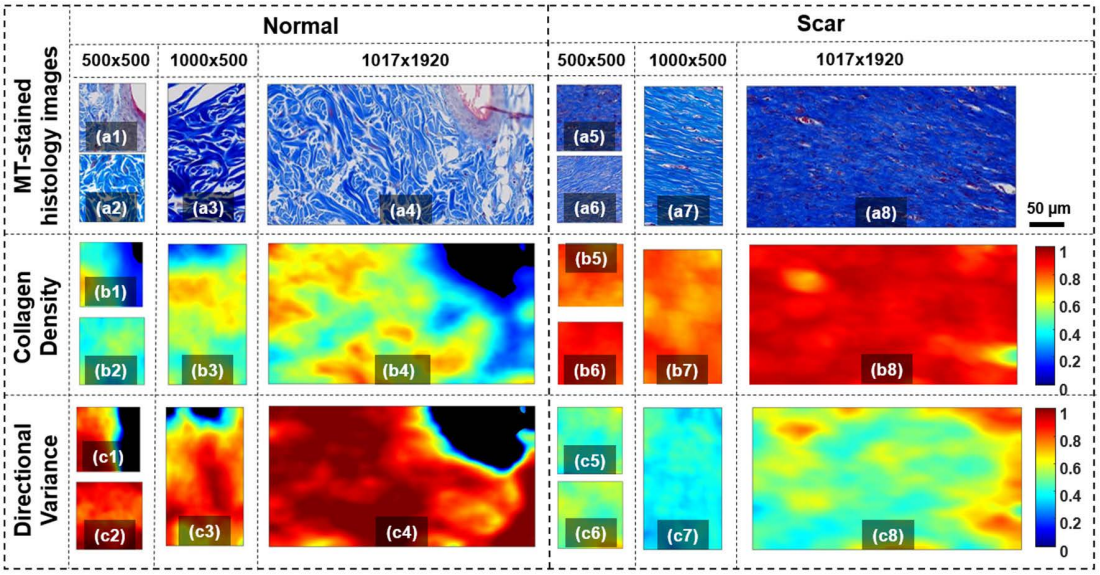

FIGURE 8. Comparison between MT-stained normal tissue (left column) and scar tissue (right column) in differently sized patches (500 × 500 pixels, 1000 × 500 pixels, and 1017 × 1920 pixels) of the MT-stained histology image: (a1–a4) for normal tissue and (a5–a8) for scar tissue. (b1–b8) collagen density map and (c1–c8) directional variance map.

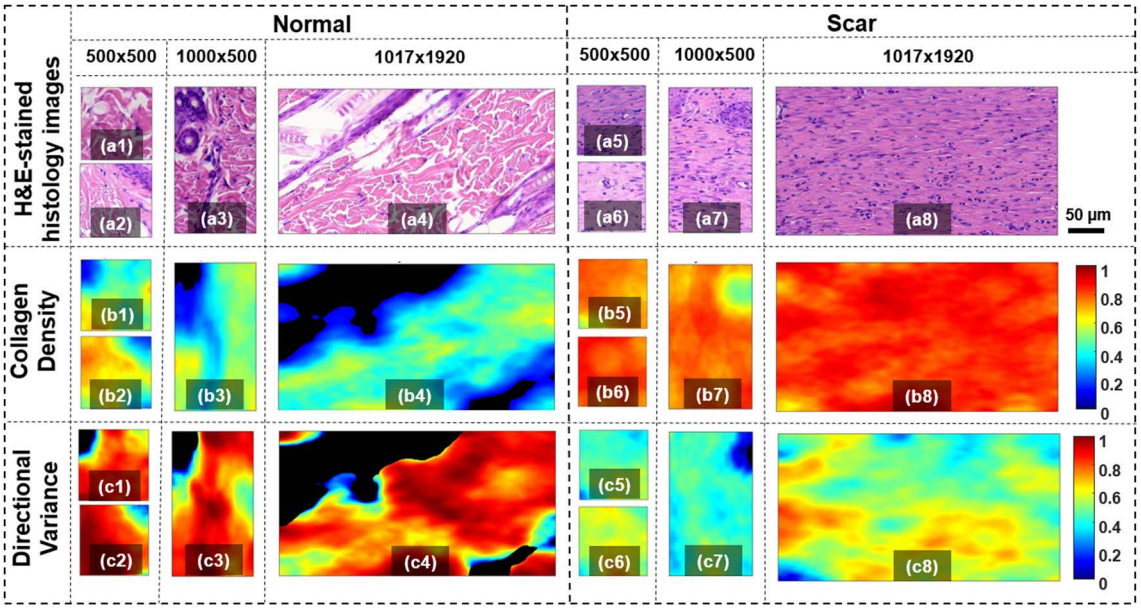

FIGURE 9. Comparison between H&E-stained normal tissue (left column) and scar tissue (right column) in differently sized patches (500 × 500 pixels, 1000 × 500 pixels, and 1017 × 1920 pixels) of the H&E-stained histology image: (a1–a4) for normal tissue and (a5–a8) for scar tissue. (b1–b8) collagen density map, and (c1–c8) directional variance map.

B. HUE-SATURATION SPECIFICITY ANALYSIS

The upper rows of Figs. 7(a–c) show the monochrome activation images obtained as a result of the hue-saturation specificity analysis performed using the features of the block1-pool layer, while varying the color hues (i.e., x-axis) and saturation (i.e., y-axis) between 0 and 1. The color bar shows the range of monochrome activation. The lower rows of Figs. 7(a–c) show the corresponding feature maps of the sample histology images in Fig. 4 (Figs. 4 (a), (c): normal and (b), (d): scar). Fig. 5(a) shows the feature maps 8, 28, and 53 selected for the MT-stained images based on the results of a hue specificity analysis. These features, the high activation spectrum of which was in the range of green to blue color (corresponding hue: 0.2–0.8), illustrate the collagen regions at higher activation levels (brighter pixels) and the background and other structures at lower activation levels (darker pixels). For the H&E-stained images, Fig. 7(b) shows the feature maps 19, 46, and 53 from the top three activations and the corresponding activated spectrum in the H&E-staining color range (blue (nucleic)-pink (collagen)-red (blood cells), corresponding hues: 0.6–1 and 0–0.2). Features 3 and 52 (Fig. 7(c)) with activation in blue and dark purple

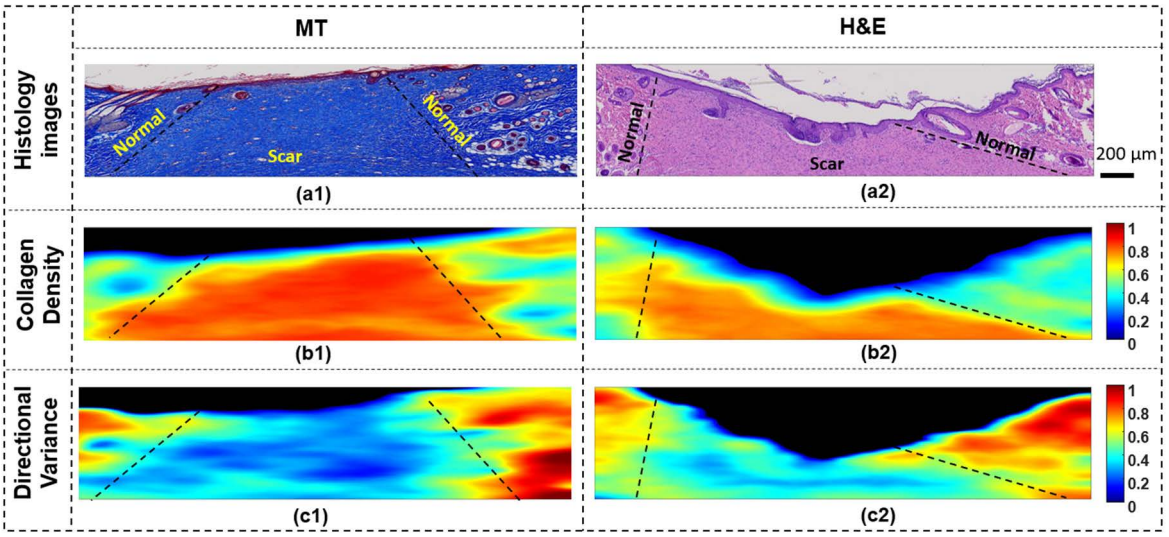

FIGURE 10. Characterization of normal tissue and scar tissue for whole histology image: (a1, a2) MT-stained (left column) and H&E-stained (right column) histology images, and the corresponding (b1, b2) collagen density maps and (c1, c2) directional variance maps.

(corresponding hue: 0.6–0.8) were selected to exclude the region with other structures, as illustrated in Fig. 7(c).

C. CHARACTERIZATION OF COLLAGEN FIBERS

Figs. 8 and 9 illustrates the characterization results of the MT-stained images (Figs. 8(a1–a4) for normal tissue and (a5–a8) for scar tissue) and H&E-stained images (Figs. 9 (a1–a4) for normal tissue and (a5–a8) for scar tissue) of various input sizes. Regarding collagen density, Figs. 8(b1–b8) and Figs. 9(b1–b8) represent the density maps corresponding to the histology images shown in Figs. 8 (a1–a8) and Figs. 9 (a1–a8). Overall, the collagen density values of the normal tissue (Figs 8 (b1–b4) and Figs. 9 (b1–b4)) are lower than those of the scar tissue (Figs. 8 (b5–b8) and Figs. 9 (b5–b8)) by 42% and 39%, respectively. Finally, Figs. 8 (c1–c8) and Figs. 9 (c1–c8) show the directional variance of the images shown in Figs. 8 (a1–a8) and Figs. 9 (a1–a8), as determined using the proposed method. The mean of directional variance of the normal tissue is significantly higher (42%) than that of the scar tissue in the cases of the MT- and H&E-stained images.

The whole histology image of the MT- and H&E-stained tissues (Figs. 10 (a1, a2)) containing both normal and scar regions was used to visualize the collagen density and directional variance. The scar region (middle) contained denser and more well-oriented collagen than the normal regions (left and right sides in Figs. 10 (a1, a2)). The collagen density was higher in the scar tissue region (Figs. 10 (b1, b2)). The scar tissue in the middle of the images exhibited significantly low directional variance, meaning that the collagen fibers were more aligned with each other (Figs. 9 (c1, c2)).

D. STATISTICAL ANALYSIS

Fig. 11 presents the results of a statistical analysis of the collagen density and directional variances extracted from the histology images obtained using two different staining methods (left: MT-stained, right: H&E-stained). The bar graphs presented in Figs. 11(a) and (b) show the means of density and directional variance, respectively. The mean collagen density of the normal tissue (0.47 ± 0.086) is 38% lower than that of the scar tissue (0.76 ± 0.067) owing to an increase in the amount of denser collagen fibers during tissue re-epithelization. The normal tissue with a basket weave-like collagen fiber pattern has randomly distributed collagen bundles. Thus, the mean of directional variance of fibers in the normal tissue, as extracted using the proposed method, is 0.67 ± 0.139. By contrast, the collagen fibers in the scar tissue are aligned; therefore, the directional variance of collagen fibers in the scar tissue is noticeably lower (0.44 ± 0.083) than that in the normal tissue. The directional variance of the scar tissue is significantly lower (34%) than that of the normal tissue. All comparisons of density and directional variance of the histology images of normal and scar tissues have a significant p-value ($p < 0.001$) in terms of the Wilcoxon signed rank statistics.

In a statistical comparison between the results of the present and previous studies, the scar tissues stained using the two staining methods were not significantly different ($p > 0.05$) in terms of density and directional variance. In case of the normal tissue, the mean density determined using the previous approach was significantly higher than that determined using the proposed approach ($p < 0.001$). By contrast, the directional variance determined using the previous approach was significantly lower than that determined using the proposed approach ($p < 0.001$). These results demonstrated that the proposed UCNN model enhances the discrimination between scar tissue and normal tissue, with a greater difference in characterization (i.e., density and directional variance).

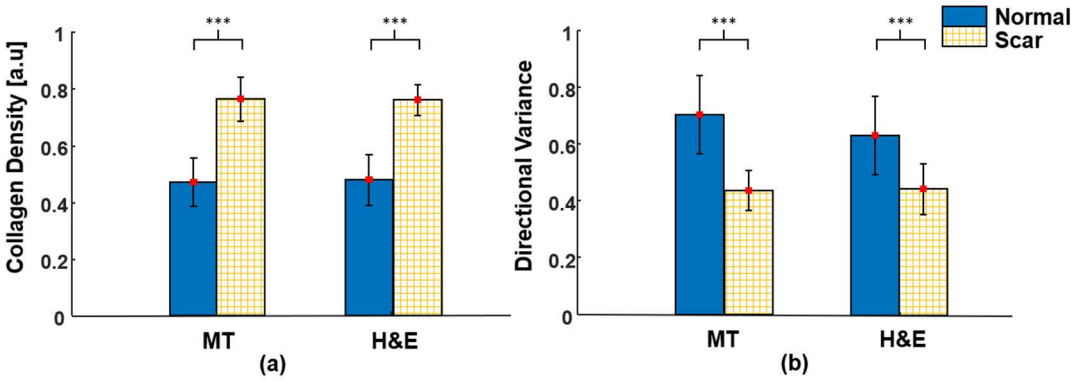

FIGURE 11. Statistical analysis of (a) collagen densities and (b) directional variances in the characterization of MT- and H&E-stained histology images (***$p < 0.05$ for normal vs. scar tissue).

IV. DISCUSSION

In the present study, we demonstrated the ability of the proposed UCNN model in terms of both classification and characterization of MT- and H&E-stained histology images. The results of our previous study proved that collagen organization can be clearly differentiated and characterized using MT-stained histology images [13]. However, distinguishing collagen organization using H&E-stained histology images remained challenging owing to the narrow derivation of the staining color. Although the color components of various staining methods are different, the tissue structures remain the same. Thus, we proposed a UCNN model and a method for visually characterizing histology images, regardless of the staining method (i.e., H&E and MT staining in this study). In addition, the classification results indicated that the proposed UCNN model could extract the primary features of tissues to differentiate between normal and scar tissues (accuracy $> 97\%$), regardless of the staining method used. To prove the multi-scalability of the proposed model, test and training image data of different sizes were used, as summarized in Table 1. Because it was not possible to split the data into several groups under the same condition (i.e., image size), cross validation [49], such as k-fold or Monte Carlo, was inapplicable. Given that we had a sufficient amount of data, a large test dataset was utilized instead to validate the network. The performance of the proposed network confirmed that it was trained well with a small amount of training data.

The EfficientNetB0 and EfficientNetB2 models yielded adequate classification performance. Also, advanced models with higher image resolutions, such as EfficientNetB7 [39], can also be trained to achieve improved classification performance. However, the architectures of the advanced models are rather complicated from the viewpoint of extracting features for characterization purposes. It will be further investigated to utilize the advanced models for the characterization. The performance of SVM was worse than those of EfficientNetB0, EfficientNetB2, and the proposed model. SVM and EfficientNet can be further optimized by tuning its hyperparameters by using the grid search tool [50]. However, this is beyond the scope of the present study, which focuses on classification and feature extraction for characterization from the DL model. The results of the present study indicate that the color- and texture-based features obtained using the proposed model can be utilized to analyze the organization of collagen bundles. The collagen densities of normal and scar tissues, as extracted using the proposed method, differ significantly (38%). In addition, directional variance, which is the strongest differentiator of collagen fiber organization post tissue remodeling after a burn injury, decreased notably (34%) for the scar tissue than it did for the normal tissue. The results of this study indicate that the proposed approach that utilizes the features extracted using the proposed UCNN model can possibly replace expensive tissue characterization methods.

While we used only RGB color features in the previous study [13], herein, we conducted a hue-saturation specificity analysis. Hue-saturation specificity analysis helps one to extract color features. Thus, the main color components of the histology images examined in the 2D histogram analysis (Fig. 4) could be selected from the extracted color features (Fig. 7). In this light, we developed a universal model for two different staining methods that represent various tissue structures with different colors. The model utilized the first two blocks pre-trained using ImageNet because they were observed to be highly sensitive to the color of the input images, which is a prominent feature for extracting a collagen mask. To extract the specific color features of the histology images, we used three steps. First, hue-saturation specificity analysis was performed to visualize the color features (hue and saturation) from the network (Fig. 7). Next, the main color components (hue and saturation) of the collagen area in the MT- and H&E- stained histology images were determined from 2D histogram analysis (Fig. 4). Finally, the matching color features between the hue-saturation specificity analysis and the 2D histogram analysis were selected for MT- (features 7, 28, and 53) and H&E- (features 19, 46, and 53) stained images, respectively. Although the

histogram of the example MT-stained images used in this study (Figs. 4 (a, b)) contained collagen areas stained with a strong shade of blue (i.e., hue $>$ 0.5), the collagen areas in the MT-stained images ranged from green to blue in color (i.e., hue: 0.2–0.8) owing to variations in the staining process [7]. Thus, hue features ranging from 0.2 to 0.8 were included in the feature map (Fig. 7). In addition, it was observed that the characterization process deteriorated when the image saturation was low ($<$ 0.4) because the color representing collagen was extremely close to white color, and the hue colors were diminished (Fig. 4(e)). Thus, the sigmoid function (Eq. (1)) was applied to compensate for the decrease in saturation based on a linear regression between saturation and activation of the extracted features. According to the slope (k_1 in Eq. (2)), the MT-stained histology images were less affected by saturation than the H&E-stained histology images. The results obtained using the proposed UCNN model demonstrated that variations in the histology staining process (e.g., color variation) did not compromise the classification and characterization performance of the proposed model. Further investigations with broader variations in the staining and scanning processes are necessary. Given that the training images were resized to the input size of 224 $\times$ 224 pixels to facilitate utilization of the pre-trained network weights, the performance of the proposed UCNN model can be degraded when it is applied to images with resolutions higher (i.e., 1000 õ 500, 1017 õ 1920, and 500 õ 500) than that of the input images. However, the results of this study proved that the trained model performed adequately well in terms of classification and characterization when applied to multi-scale images.

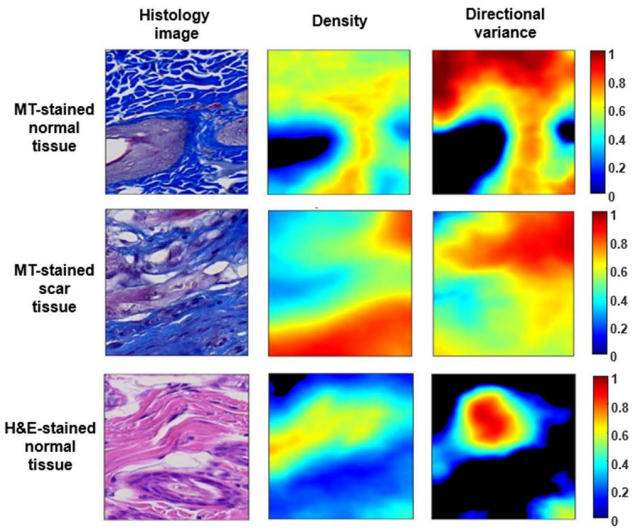

FIGURE 12. Misclassified cases for MT-stained normal and scar tissues and H&E-stained normal tissue (from top to bottom) and the corresponding density and directional variance.

As demonstrated by the confusion matrices (Figs. 6 (d, e)), the proposed UCNN model mislabeled a few test instances. Fig. 12 showed examples of the misclassified cases, including MT-stained normal and scar tissues and H&E-stained normal tissues. It is observed that these histology images contain smaller proportions of collagen than the other structures, such as glandular cells and follicles. Although misclassified, the characterization results (density and directional variance) obtained in these cases are acceptable. This confirms that the proposed model learns and differentiates the features properly, regardless of the staining method. Further investigation is necessary to understand whether the misclassified cases affect the characterization performance of the proposed approach.

While the color-based features of the collagenous regions in the MT- and H&E-stained images could be selected using the results of the hue-saturation specificity analysis (Figs. 4 and 7), the texture-based features representing the directional variance could be extracted from the last convolution layer. Our observations in this study were consistent with our expectation that as the tissue undergoes remodeling, the collagen fibers are organized in a denser and more aligned manner in terms of their distribution and orientation. Moreover, the proposed approach can be applied to whole histology images for characterization, as illustrated in Fig. 10.

For the proposed UCNN model, it was observed that the color-based features constituted the key factor in both classification and characterization. The proposed model utilized RGB color images that were augmented in the HSV color space. In future studies, DL models using input images in color spaces other than the RGB color space (e.g., HSV, CIELAB) can be investigated [51], [52]. For color augmentation, color normalization methods, including color deconvolution and various DL models, can be utilized [33], [36], [37]. Furthermore, an extended universal model for the classification and characterization of histology images obtained using other staining methods (e.g., picrosirius red, Movat's pentachrome) will be investigated [53], [54]. Although the current study was limited to differentiation and characterization between two categories (i.e., normal tissue and scar tissue), it can be extended to various types of scars such as normal, keloid, hypertrophic, and depressed scars that are formed after a burn injury [4]. In the future, we intend to investigate collagen quantification for distinguishing other types of scars. For clinical and prognostic applications, it is important to exploit the characteristics of collagen fiber organization to intergrade information related to various pathological studies, including cancer, aging, wound healing, and diabetes [9]–[11], [31]. In this regard, the promising results obtained herein demonstrate the competence of the proposed model in assisting pathologists to achieve prompt and accurate diagnoses.

V. CONCLUSION

The proposed UCNN can classify and characterize collagen organization after tissue remodeling by using MT- and H&E-stained histology images. Regardless of the staining method in use, we were able to utilize the proposed model to extract significant features for characterization by employing

the results of hue-saturation specificity analysis. In the future, we will extend the proposed UCNN model to various staining methods and ensure that it can stage scars for quantitative assessments in clinical scar treatment.

ACKNOWLEDGMENT

The authors thank Seyeon Park for her language editing.

REFERENCES

[1] P. Monika, P. V. Waiker, M. N. Chandraprabha, A. Rangarajan, and K. N. C. Murthy, "Myofibroblast progeny in wound biology and wound healing studies," *Wound Repair Regener.*, vol. 29, no. 4, pp. 531–547, May 2021, doi: 10.1111/wrr.12937.

[2] L. E. Tracy, R. A. Minasian, and E. J. Caterson, "Extracellular matrix and dermal fibroblast function in the healing wound," *Adv. Wound Care*, vol. 5, no. 3, pp. 119–136, Mar. 2016, doi: 10.1089/wound.2014.0561.

[3] T. Velnar, T. Bailey, and V. Smrkolj, "The wound healing process: An overview of the cellular and molecular mechanisms," *J. Int. Med. Res.*, vol. 37, no. 5, pp. 1528–1542, Sep./Oct. 2009, doi: 10.1177/147323000903700531.

[4] M. Xue and C. J. Jackson, "Extracellular matrix reorganization during wound healing and its impact on abnormal scarring," *Adv. Wound Care*, vol. 4, no. 3, pp. 119–136, Mar. 2015, doi: 10.1089/wound.2013.0485.

[5] J. M. Rawlins, W. L. Lam, R. O. Karoo, I. L. Naylor, and D. T. Sharpe, "Quantifying collagen type in mature burn scars: A novel approach using histology and digital image analysis," *J. Burn Care Res.*, vol. 27, no. 1, pp. 60–65, Jan./Feb. 2006, doi: 10.1097/01.bcr.0000192266.14329.7b.

[6] M. Titford, "Progress in the development of microscopical techniques for diagnostic pathology," *J. Histotechnol.*, vol. 32, no. 1, pp. 9–19, 2009, doi: 10.1179/014788809794748024.

[7] M. H. Flint, M. F. Lyons, M. F. Meaney, and D. E. Williams, "The Masson staining of collagen—An explanation of an apparent paradox," *Histochem. J.*, vol. 7, no. 6, pp. 529–546, Nov. 1975, doi: 10.1007/BF01003791.

[8] G. Litjens, C. I. Sánchez, N. Timofeeva, M. Hermsen, I. Nagtegaal, I. Kovacs, C. H.-V. De Kaa, P. Bult, B. Van Ginneken, and J. Van Der Laak, "Deep learning as a tool for increased accuracy and efficiency of histopathological diagnosis," *Sci. Rep.*, vol. 6, p. 26286, May 2016, doi: 10.1038/srep26286.

[9] C. R. Drifka, A. G. Loeffler, K. Mathewson, A. Keikhosravi, J. C. Eickhoff, Y. Liu, S. M. Weber, W. J. Kao, and K. W. Eliceiri, "Highly aligned stromal collagen is a negative prognostic factor following pancreatic ductal adenocarcinoma resection," *Oncotarget*, vol. 7, no. 46, pp. 76197–76213, Nov. 2016, doi: 10.18632/oncotarget.12772.

[10] M. W. Conklin, J. C. Eickhoff, K. M. Riching, C. A. Pehlke, K. W. Eliceiri, P. P. Provenzano, A. Friedl, and P. J. Keely, "Aligned collagen is a prognostic signature for survival in human breast carcinoma," *Amer. J. Pathol.*, vol. 178, no. 3, pp. 1221–1232, Mar. 2011, doi: 10.1016/j.ajpath.2010.11.076.

[11] A. Keikhosravi, B. Li, Y. Liu, M. W. Conklin, A. G. Loeffler, and K. W. Eliceiri, "Non-disruptive collagen characterization in clinical histopathology using cross-modality image synthesis," *Commun. Biol.*, vol. 3, no. 1, p. 414, Jul. 2020, doi: 10.1038/s42003-020-01151-5.

[12] A. Suvik and A. W. Effendy, "The use of modified Masson's trichrome staining in collagen evaluation in wound healing study," *Malaysian J. Vet. Res.*, vol. 3, no. 1, pp. 39–47, Jan. 2012.

[13] T. T. A. Pham, H. Kim, Y. Lee, H. W. Kang, and S. Park, "Deep learning for analysis of collagen fiber organization in scar tissue," *IEEE Access*, vol. 9, pp. 101755–101764, 2021, doi: 10.1109/access.2021.3097370.

[14] K. P. Quinn, A. Golberg, G. F. Broelsch, S. Khan, M. Villiger, B. Bouma, W. G. Austen, R. L. Sheridan, M. C. Mihm, M. L. Yarmush, and I. Georgakoudi, "An automated image processing method to quantify collagen fibre organization within cutaneous scar tissue," *Exp. Dermatol.*, vol. 24, no. 1, pp. 78–80, Jan. 2015, doi: 10.1111/exd.12553.

[15] J. K. C. Chan, "The wonderful colors of the Hematoxylin–Eosin stain in diagnostic surgical pathology," *Int. J. Surgical Pathol.*, vol. 22, no. 1, pp. 12–32, Feb. 2014, doi: 10.1177/1066896913517939.

[16] C. Bayan, J. M. Levitt, E. Miller, D. Kaplan, and I. Georgakoudi, "Fully automated, quantitative, noninvasive assessment of collagen fiber content and organization in thick collagen gels," *J. Appl. Phys.*, vol. 105, no. 10, May 2009, Art. no. 102042, doi: 10.1063/1.3116626.

[17] Y. V. Kistenev, D. A. Vrazhnov, V. V. Nikolaev, E. A. Sandykova, and N. A. Krivova, "Analysis of collagen spatial structure using multiphoton microscopy and machine learning methods," *Biochemistry*, vol. 84, no. S1, pp. 108–123, Jan. 2019, doi: 10.1134/S0006297919140074.

[18] K. P. Quinn and I. Georgakoudi, "Rapid quantification of pixel-wise fiber orientation data in micrographs," *J. Biomed. Opt.*, vol. 18, no. 4, Apr. 2013, Art. no. 046003, doi: 10.1117/1.JBO.18.4.046003.

[19] L. Schmarje, C. Zelenka, U. Geisen, C.-C. Glüer, and R. Koch, "2D and 3D segmentation of uncertain local collagen fiber orientations in SHG microscopy," in *Pattern Recognition*. Cham, Switzerland: Springer, 2019, pp. 374–386.

[20] X. Jiang, J. Zhong, Y. Liu, H. Yu, S. Zhuo, and J. Chen, "Two-photon fluorescence and second-harmonic generation imaging of collagen in human tissue based on multiphoton microscopy," *Scanning*, vol. 33, no. 1, pp. 53–66, Jan./Feb. 2011, doi: 10.1002/sca.20219.

[21] P. A. Bautista and Y. Yagi, "Multispectral enhancement method to increase the visual differences of tissue structures in stained histopathology images," *Anal. Cellular Pathol.*, vol. 35, nos. 5–6, pp. 407–420, 2012, doi: 10.3233/ACP-2012-0069.

[22] P. P. van Zuijlen, H. J. C. de Vries, E. N. Lamme, J. E. Coppens, J. Van Marle, R. W. Kreis, and E. Middelkoop, "Morphometry of dermal collagen orientation by Fourier analysis is superior to multi-observer assessment," *J. Pathol.*, vol. 198, no. 3, pp. 284–291, Nov. 2002, doi: 10.1002/path.1219.

[23] V. Marcos-Garces, M. Harvat, P. M. Aguilar, A. F. Izquierdo, and A. Ruiz-Sauri, "Comparative measurement of collagen bundle orientation by Fourier analysis and semiquantitative evaluation: Reliability and agreement in Masson's trichrome, Picrosirius red and confocal microscopy techniques," *J. Microsc.*, vol. 267, no. 2, pp. 130–142, Aug. 2017, doi: 10.1111/jmi.12553.

[24] F. Fereidouni, A. Todd, Y. Li, C.-W. Chang, K. Luong, A. Rosenberg, Y.-J. Lee, J. W. Chan, A. Borowsky, K. Matsukuma, K.-Y. Jen, and R. Levenson, "Dual-mode emission and transmission microscopy for virtual histochemistry using hematoxylin- and eosin-stained tissue sections," *Biomed. Opt. Exp.*, vol. 10, no. 12, pp. 6516–6530, Dec. 2019, doi: 10.1364/BOE.10.006516.

[25] T. Ching *et al.*, "Opportunities and obstacles for deep learning in biology and medicine," *J. R Soc. Interface*, vol. 15, no. 141, Apr. 2018, Art. no. 20170387, doi: 10.1098/rsif.2017.0387.

[26] D. Komura and S. Ishikawa, "Machine learning methods for histopathological image analysis," *Comput. Struct. Biotechnol. J.*, vol. 16, pp. 34–42, Jan. 2018, doi: 10.1016/j.csbj.2018.01.001.

[27] G. Litjens, T. Kooi, B. E. Bejnordi, A. A. A. Setio, F. Ciompi, M. Ghafoorian, J. A. Van Der Laak, B. Van Ginneken, and C. I. Sánchez, "A survey on deep learning in medical image analysis," *Med. Image Anal.*, vol. 42, pp. 60–88, Dec. 2017, doi: 10.1016/j.media.2017.07.005.

[28] D. Ravi, C. Wong, F. Deligianni, M. Berthelot, J. Andreu-Perez, B. Lo, and G.-Z. Yang, "Deep learning for health informatics," *IEEE J. Biomed. Health Inform.*, vol. 21, no. 1, pp. 4–21, Jan. 2017, doi: 10.1109/JBHI.2016.2636665.

[29] J. van der Laak, G. Litjens, and F. Ciompi, "Deep learning in histopathology: The path to the clinic," *Nature Med.*, vol. 27, no. 5, pp. 775–784, May 2021, doi: 10.1038/s41591-021-01343-4.

[30] N. Tajbakhsh, J. Y. Shin, S. R. Gurudu, R. T. Hurst, C. B. Kendall, M. B. Gotway, and J. Liang, "Convolutional neural networks for medical image analysis: Full training or fine tuning?" *IEEE Trans. Med. Imag.*, vol. 35, no. 5, pp. 1299–1312, May 2016, doi: 10.1109/TMI.2016.2535302.

[31] J. Isaksson, I. Arvidsson, K. Åaström, and A. Heyden, "Semantic segmentation of microscopic images of H&E stained prostatic tissue using CNN," in *Proc. Int. Joint Conf. Neural Netw. (IJCNN)*, May 2017, pp. 1252–1256.

[32] X. Fu, T. Liu, Z. Xiong, B. H. Smaill, M. K. Stiles, and J. Zhao, "Segmentation of histological images and fibrosis identification with a convolutional neural network," *Comput. Biol. Med.*, vol. 98, pp. 147–158, Jul. 2018, doi: 10.1016/j.compbiomed.2018.05.015.

[33] A. Khan, M. Atzori, S. Otálora, V. Andrearczyk, and H. Müller, "Generalizing convolution neural networks on stain color heterogeneous data for computational pathology," *Proc. SPIE*, vol. 11320, Mar. 2020, Art. no. 113200R.

[34] D. Tellez, G. Litjens, P. Bándi, W. Bulten, J.-M. Bokhorst, F. Ciompi, and J. van der Laak, "Quantifying the effects of data augmentation and stain color normalization in convolutional neural networks for computational pathology," *Med. Image Anal.*, vol. 58, Dec. 2019, Art. no. 101544, doi: 10.1016/j.media.2019.101544.

[35] A. C. Ruifrok and D. A. Johnston, "Quantification of histochemical staining by color deconvolution," *Anal. Quantum Cytol, Histol.*, vol. 23, no. 4, pp. 291–299, Aug. 2001.
[36] M. Macenko, M. Niethammer, J. S. Marron, D. Borland, J. T. Woosley, X. Guan, C. Schmitt, and N. E. Thomas, "A method for normalizing histology slides for quantitative analysis," in *Proc. IEEE Int. Symp. Biomed. Imag., From Nano Macro*, Jun./Jul. 2009, pp. 1107–1110.
[37] A. M. Khan, N. Rajpoot, D. Treanor, and D. Magee, "A nonlinear mapping approach to stain normalization in digital histopathology images using image-specific color deconvolution," *IEEE Trans. Biomed. Eng.*, vol. 61, no. 6, pp. 1729–1738, Jun. 2014, doi: 10.1109/TBME.2014.2303294.
[38] K. Simonyan and A. Zisserman, "Very deep convolutional networks for large-scale image recognition," 2015, *arXiv:1409.1556*.
[39] M. Tan and Q. Le, "EfficientNet: Rethinking model scaling for convolutional neural networks," presented at the 36th Int. Conf. Mach. Learn., 2019. [Online]. Available: https://proceedings.mlr.press/v97/tan19a.html
[40] C.-C. Chang and C.-J. Lin, "LIBSVM," *ACM Trans. Intell. Syst. Technol.*, vol. 2, no. 3, pp. 1–27, 2011, doi: 10.1145/1961189.1961199.
[41] D. G. Lowe, "Distinctive image features from scale-invariant keypoints," *Int. J. Comput. Vis.*, vol. 60, no. 2, pp. 91–110, Mar. 2004, doi: 10.1023/B:VISI.0000029664.99615.94.
[42] T. Kanungo, D. M. Mount, N. S. Netanyahu, C. D. Piatko, R. Silverman, and A. Y. Wu, "An efficient K-means clustering algorithm: Analysis and implementation," *IEEE Trans. Pattern Anal. Mach. Intell.*, vol. 24, no. 7, pp. 881–892, Jul. 2002, doi: 10.1109/TPAMI.2002.1017616.
[43] S. O'Hara and B. A. Draper, "Introduction to the bag of features paradigm for image classification and retrieval," 2011, *arXiv:1101.3354*.
[44] T. Fawcett, "An introduction to ROC analysis," *Pattern Recognit. Lett.*, vol. 27, no. 8, pp. 861–874, Jun. 2005, doi: 10.1016/j.patrec.2005.10.010.
[45] M. Engilberge, E. Collins, and S. Süsstrunk, "Color representation in deep neural networks," in *Proc. IEEE Int. Conf. Image Process. (ICIP)*, Sep. 2017, pp. 2786–2790.
[46] N. Otsu, "A threshold selection method from gray-level histograms," *IEEE Trans. Syst., Man, Cybern.*, vol. SMC-9, no. 1, pp. 62–66, Jan. 1979.
[47] A. P. King and R. J. Eckersley, "Inferential statistics III: Nonparametric hypothesis testing," in *Statistics for Biomedical Engineers and Scientists*. Amsterdam, The Netherlands: Elsevier, 2019, pp. 119–145.
[48] G. D. Ruxton and M. Neuhäuser, "When should we use one-tailed hypothesis testing?" *Methods Ecol. Evol.*, vol. 1, no. 2, pp. 114–117, Jun. 2010, doi: 10.1111/j.2041-210X.2010.00014.x.
[49] D. Berrar, "Cross-validation," in *Encyclopedia of Bioinformatics and Computational Biology*. Amsterdam, The Netherlands: Elsevier, 2019, pp. 542–545.
[50] A. Rosebrock. *Grid Search Hyperparameter Tuning With Scikit-Learn (GridSearchCV)*. Accessed: Dec. 17, 2021. [Online]. Available: https://www.pyimagesearch.com/2021/05/24/grid-search-hyperparameter-tuning-with-scikit-learn-gridsearchcv/
[51] P. Bautista, N. Hashimoto, and Y. Yagi, "Color standardization in whole slide imaging using a color calibration slide," *J. Pathol. Informat.*, vol. 5, no. 1, p. 4, 2014, doi: 10.4103/2153-3539.126153.
[52] A. R. Smith, "Color gamut transform pairs," presented at the 5th Annu. Conf. Comput. Graph. Interact. Techn. (SIGGRAPH), 1978.
[53] P. G. B. Coelho, M. V. D. Souza, L. G. Conceição, M. I. V. Viloria, and S. A. O. Bedoya, "Evaluation of dermal collagen stained with picrosirius red and examined under polarized light microscopy," *Anais Brasileiros de Dermatologia*, vol. 93, no. 3, pp. 415–418, 2018, doi: 10.1590/abd1806-4841.20187544.
[54] K. Doello, "A new pentachrome method for the simultaneous staining of collagen and sulfated mucopolysaccharides," *Yale J. Biol. Med.*, vol. 87, no. 3, pp. 341–347, Sep. 2014.

THI TRAM ANH PHAM received the B.S. degree in physics engineering from the Ho Chi Minh City University of Technology, Vietnam, in 2018, and the M.S. degree from the School of Electrical and Electronics Engineering, Chung-Ang University, Seoul, Republic of Korea, in 2021. Her research interests include biomedical signal and image analysis, deep learning, and model extraction.

HYEONSOO KIM received the B.S. degree in biomedical engineering from Pukyong National University, Busan, Republic of Korea, in 2020. He is working on picoseond laser therapy for treating melasoma.

YEACHAN LEE received the B.S. and M.S. degrees in biomedical engineering from Pukyong National University, Busan, Republic of Korea, in 2018 and 2020, respectively, where he is currently pursuing the Ph.D. degree on laser therapy for fibrotic diseases and development of endoscopic applicators.

HYUN WOOK KANG received the B.S. degree in mechanical engineering from Yonsei University, Republic of Korea, in 2002, and the M.S. degree in mechanical engineering and the Ph.D. degree in biomedical engineering from The University of Texas at Austin, Austin, TX, USA, in 2004 and 2006, respectively.

From 2002 to 2006, he was a Research Assistant with the Biomedical Engineering Laser Laboratory. In 2007, he joined the Laser Therapeutics Research Laboratory, American Medical Systems, San Jose, CA, USA, and worked as a Senior Research Scientist on advanced laser therapy of urological diseases. Since 2012, he has been a Professor with the Biomedical Engineering Department, Pukyong National University, Busan, Republic of Korea. He is the author of more than 100 articles and more than 30 inventions. His research interests include laser-tissue interactions, multifunctional endoscopic laser treatment, design of disease-targeted therapeutics, and commercialization of biomedical devices. He has been the Conference Chair of the Urology Program at SPIE BiOS.

SUHYUN PARK (Member, IEEE) received the B.S. and M.S. degrees in electronic engineering from Ewha Womans University, Seoul, Republic of Korea, in 1999 and 2001, respectively, and the Ph.D. degree in biomedical engineering from The University of Texas at Austin, Austin, TX, USA, in 2008.

From 2003 to 2008, she worked as a Research Assistant at the Ultrasound and Therapeutic Research Laboratory. In 2008, she joined the Imaging Technology Group, GE Global Research, Niskayuna, NY, USA, and worked as a Scientist and Systems Engineer on advanced ultrasound imaging applications. In 2012, she joined the Samsung Advanced Institute of Technology, Suwon, Gyeonggi, Republic of Korea, and worked as a Research Staff Member. From 2017 to 2020, she was a Professor with the School of Electrical and Electronics Engineering, Chung-Ang University, Seoul. Since 2021, she has been a Professor with the Department of Electronic and Electrical Engineering, Ewha Womans University. She has authored more than 60 articles and patented more than ten inventions. Her research interests include intelligent sensing and processing techniques, ultrasound imaging, and biosignal analysis.